Freezing lines of colloidal Yukawa spheres. II. Local structure and characteristic lengths

Jacek Gapinski, Gerhard Nägele, and Adam Patkowski

Articles you may be interested in

Freezing lines of colloidal Yukawa spheres. I. A Rogers-Young integral equation study
J. Chem. Phys. **136**, 024507 (2012); 10.1063/1.3675607

Pair structure of the hard-sphere Yukawa fluid: An improved analytic method versus simulations, Rogers-Young scheme, and experiment
J. Chem. Phys. **134**, 044532 (2011); 10.1063/1.3524309
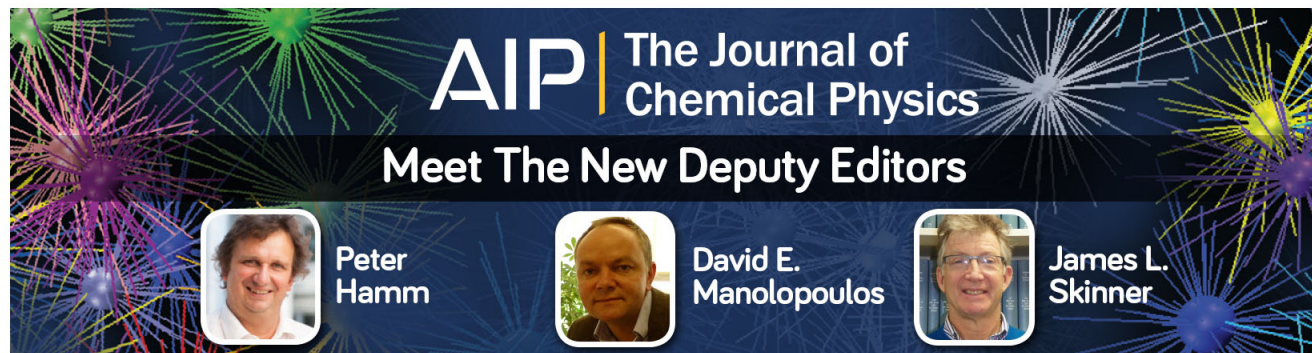
Freezing of charged colloids in slit pores
J. Chem. Phys. **129**, 244703 (2008); 10.1063/1.3046565

Collective diffusion, self-diffusion and freezing criteria of colloidal suspensions
J. Chem. Phys. **113**, 3381 (2000); 10.1063/1.1286964

Theoretical problems in the crystallization of hard sphere colloidal particles
AIP Conf. Proc. **519**, 11 (2000); 10.1063/1.1291517

Freezing lines of colloidal Yukawa spheres. II. Local structure and characteristic lengths

Jacek Gapinski,[1,2,a)] Gerhard Nägele,[3] and Adam Patkowski[1,2]

[1]*Molecular Biophysics Division, Faculty of Physics, A. Mickiewicz University, Umultowska 85, 61-614 Poznań, Poland*
[2]*NanoBioMedical Center, A. Mickiewicz University, Umultowska 85, 61-614 Poznań, Poland*
[3]*Institute of Complex Systems (ICS-3), Forschungszentrum Jülich, D-52425 Jülich, Germany*

Using the Rogers-Young (RY) integral equation scheme for the static pair correlation functions combined with the liquid-phase Hansen-Verlet freezing rule, we study the generic behavior of the radial distribution function and static structure factor of monodisperse charge-stabilized suspensions with Yukawa-type repulsive particle interactions at freezing. In a related article, labeled Paper I [J. Gapinski, G. Nägele, and A. Patkowski, J. Chem. Phys. **136**, 024507 (2012)], this hybrid method was used to determine two-parameter freezing lines for experimentally controllable parameters, characteristic of suspensions of charged silica spheres in dimethylformamide. A universal scaling of the RY radial distribution function maximum is shown to apply to the liquid-bcc and liquid-fcc segments of the universal freezing line. A thorough analysis is made of the behavior of characteristic distances and wavenumbers, next-neighbor particle coordination numbers, osmotic compressibility factor, and the Ravaché-Mountain-Streett minimum-maximum radial distribution function ratio. © *2014 AIP Publishing LLC*. [http://dx.doi.org/10.1063/1.4895965]

I. INTRODUCTION

A large variety of colloidal particles carry surface charges when dispersed in a polar solvent such as water. The electrostatic repulsion between the colloidal particles can be used to stabilize them against van der Waals attraction, and to create soft crystalline structures with applications, e.g., in photonic band gaps.[1] Examples of globular particles of technological and biological relevance range from solid anorganic and organic colloidal spheres[2–4] to soft ionic microgels[5] and proteins.[6,7] In addition to being of practical relevance, charge-stabilized colloids can serve as convenient model systems for addressing fundamental statistical physics problems, owing to the experimental viewpoint conveniently accessible colloidal time and length scales. The electrosteric part of the effective pair potential between charge-stabilized colloidal spheres is commonly modeled as a hard-sphere plus screened Yukawa potential, with the latter potential part referred to as the (repulsive) Yukawa potential. In many systems the Yukawa-type repulsion dominates (masks) residual short-range attraction and excluded volume interactions. The particles are then addressed as colloidal Yukawa particles. Regarding their equilibrium statistical mechanics properties, colloidal Yukawa particles systems at low ionic strength closely resemble dusty plasmas.[8] Yukawa colloidal suspensions have unique properties, with the crystallization process being one of the most interesting ones. This justifies an in depth study of local particle ordering at fluid-solid freezing lines such as the one presented here.

Our current mainly theoretically oriented articles, Papers I[9] and II, with Paper II used as an abbreviation of the present one, have been inspired by an earlier small angle x-ray scattering (SAXS) study of charged colloidal silica spheres suspended in dimethylformamide (DMF).[10] In this earlier work, we have analyzed the SAXS data using the Rogers-Young (RY) integral equation scheme for the static structure factor and pair distribution function of the hard-sphere plus Yukawa repulsion model system.[11] The experimental trends in the salt- and volume fraction dependencies of the SAXS data are not straightforwardly to comprehend. This has motivated us to perform an exhaustive theoretical exploration of microstructural properties of the silica spheres in DMF system, in terms of experimental control parameters including the solvent salinity, particle volume fraction, and effective particle charge. In the related previous article, Paper I, the focus was on two-parameter freezing lines. This is complemented in the present study, Paper II, by a thorough analysis of the generic behavior of the static structure factor and the associated pair distribution function at freezing.

In Paper I, we analyzed the two-parameter freezing lines of colloidal particles with repulsive Yukawa-type pair interactions for a vast range of interaction parameters, representative of charge-stabilized silica spheres suspended in DMF. The freezing lines were determined using the thermodynamically partially self-consistent Rogers-Young (RY) integral equation scheme[11] for the static structure factor $S(q)$, combined with the well-known fluid-phase Hansen-Verlet (HV) rule for the structure factor peak height, $S_f(q_m)$, signaling freezing of the (colloidal) fluid into a crystalline phase.[12,13] Here, $q = q_m$ is the scattering wavenumber location of the principal peak in $S(q)$. There exist additional one-phase criteria for the fluid-solid transition such as the Lindeman melting criterion for the relative mean-squared displacement,[14] the Ravaché-Mountain-Streett (RMS) criterion for the radial distribution

---

a)gapinski@amu.edu.pl

function (RDF) $g(r)$ at freezing,[15–17] and the entropy-based ordering criterion by Giaquinta et al.[18,19] These criteria invoke information on properties of one phase only and are implemented with comparatively little numerical effort.

There exist also dynamic fluid-phase freezing criteria such as the empirical criterion by Löwen et al. for the ratio of colloidal long-time to short-time self-diffusion coefficients[20] which has been successfully applied also for mapping out the fluid-solid freezing line of dusty plasmas.[21] In Ref. 22, the inter-relation of this dynamic criterion with the static HV criterion was discussed, and alternative dynamic freezing criteria in terms of collective diffusion coefficients have been presented, which different from the self-diffusion coefficient are straightforwardly obtained in a dynamic scattering experiment. The calculation of (long-time) diffusion coefficients is substantially more demanding than that of static properties. It is thus more economical to determine freezing lines using static criteria such as the HV rule.

Only systems with hard-core interactions masked by the soft electric repulsion have been considered in Paper I, representative for most charge-stabilized systems, and a constant HV freezing value $S_f(q_m) = 3.1$ was used. The employed screened Coulomb (i.e., Yukawa-type) effective pair potential is of the form

$$\beta u(r) = L_B Z^2 \left(\frac{e^{\kappa a}}{1 + \kappa a} \right)^2 \frac{e^{-\kappa r}}{r}, \quad r > \sigma = 2a, \qquad (1)$$

where $\beta = 1/k_B T$ (k_B—Boltzmann constant, T—temperature), r is the center-to-center pair separation, σ is the particle diameter, $L_B = e^2/(\varepsilon k_B T)$ is the Bjerrum length of the suspending fluid of static dielectric constant ε at temperature T, and Z is the effective number of elementary charges e of a colloidal sphere. The Debye screening parameter, κ, is given by

$$\kappa^2 = \frac{4\pi L_B [n|Z| + 2C_s]}{1 - \phi}. \qquad (2)$$

Here, n and C_s are the colloid and added 1-1 electrolyte number density, respectively, and the free counterions released from the colloid surfaces are assumed to be monovalent. The factor $1/(1 - \phi)$, with $\phi = (4\pi/3)na^3$ denoting the colloid volume fraction, corrects for the free volume available to the small microions. Particles dispersions which can be modeled by a Yukawa-type effective pair potential range from charge-stabilized suspensions of rigid colloidal spheres[4,23,24] to globular protein solutions[6,7] and dusty plasmas.[8,25] Soft-spheres systems such as ionic microgels are also describable on basis of a screened Coulomb-type effective pair potential, for concentrations well below the overlap volume fractions where also the HV freezing rule remains applicable.[26,27] Charged silica spheres have been used in extensive studies where the colloidal suspensions were treated as model systems for liquid undercooled metals.[28–30]

RY-HV generated freezing lines have been calculated in Paper I, for all combinations of the experimentally accessible system parameters ϕ, Z, and C_s, with values characteristic of suspensions of charged silica spheres in DMF. Due to the absence of solvent self-dissociation and carbon dioxide contamination such as in water, small values of the screening parameter can be reached with DMF as the solvent. The pur-

pose of Paper I has been to provide experimentalists with a detailed knowledge base of freezing lines depending on experimentally controllable parameters.

As discussed in Paper I, the quite differently looking, application-friendly freezing lines for the experimental parameter pairs are all equivalent, for the case of hard-sphere Yukawa systems with masked hard-core interactions (i.e., point-Yukawa systems[31]), to a single universal freezing line in the two-dimensional parameter space spanned by the reduced screening parameter $\lambda = \kappa \langle r \rangle$, and the reduced temperature $\tilde{T} = k_B T / u(\langle r \rangle)$. Here, $\langle r \rangle = n^{-1/3}$ is the mean geometric inter-particle distance, and $u(\langle r \rangle)$ is the electrostatic pair potential energy at distance $\langle r \rangle$.

The universal freezing line in the $(\lambda, \tilde{T})$ parameter space obtained in Paper I using the RY-HV criterion with constant value $S_f(q_m) = 3.1$, is found to be in good agreement with simulation[31–36] and density functional theory[37,38] predictions by various groups, and it has enabled us for extending the freezing line to values of λ substantially larger than those accessed in the simulations. We have shown in Paper I that the universal freezing line for Yukawa-like particles systems with masked hard-core interactions is only weakly sensitive to changes in the precise HV criterion value used for $S_f(q_m)$.

That the two reduced parameters $(\lambda, \tilde{T})$ suffice to completely characterize the phase diagram of point-Yukawa particles is due to the universal form,

$$\beta u(x) = \Gamma \exp[-\lambda x]/x = \frac{1}{\tilde{T}} \exp[-\lambda(x - 1)]/x, \qquad (3)$$

of the pair potential, expressed in the reduced pair distance $x = r/\langle r \rangle$, which describes charge-stabilized colloidal spheres with practically zero probability of being in direct contact with each other. Here, $\Gamma = \exp[\lambda]/\tilde{T}$ is the reduced coupling parameter. Moreover, the Ornstein-Zernike equation in units of the mean particle distance reads[39]

$$g(x) - 1 = c(x) + \int d^3 x' c(|\mathbf{x} - \mathbf{x}'|)[g(x') - 1], \qquad (4)$$

where $c(x)$ is the direct correlation function associated with the RDF $g(x)$. As a consequence of Eqs. (3) and (4), different combinations of the experimentally accessible parameters $\{L_B/\sigma, Z, C_s\sigma^3, \phi\}$ which give rise to the same state point, $(\lambda, \tilde{T})$, in the universal phase diagram, are sharing the same RDF, $g(r/\langle r \rangle)$, and static structure factor,

$$S(q\langle r \rangle) = 1 + \frac{4\pi}{q\langle r \rangle} \int\limits_0^\infty dx\, x \sin(iq\langle r \rangle x)[g(x) - 1], \qquad (5)$$

provided their arguments are expressed in units of the mean particle distance. For systems of reduced parameter points $(\lambda, \tilde{T})$ right on the universal freezing line $\tilde{T}_f(\lambda)$, the static pair functions $g_f(r)$ and $S_f(q)$, and in particular their principal peak values $g_f(r_m)$ and $S_f(q_m)$ at locations r_m and $q_m \approx 2\pi/r_m$, respectively, are solely determined by λ.

The good accuracy of the RY predictions for the $S(q)$'s and $g(r)$'s of Yukawa-type particle systems in the fluid phase, has motivated us to extend our study in Paper I by a thorough investigation of the fluid-phase, radially averaged local particle structure under freezing conditions. The purpose of the

present work is to characterize the generic (scaling) behavior of $g(r)$ at freezing, by analyzing in particular characteristic changes in the RDF in going from the lower screening fluid-bcc part where $\lambda < \lambda_t$ to the larger screening fluid-fcc part of the freezing line, where $\lambda > \lambda_t$, and to explore the characteristics of the principal peak value, $g_f(r_m)$, and the first non-zero minimum, $g_f(r_{dip})$, of $g(r)$ at freezing at the locations r_m and $r_{dip} > r_m$, respectively. Here, λ_t is the reduced screening parameter at the triple point of fluid-bcc-fcc coexistence, of value $\lambda_t = 6.9$[35] or $\lambda_t = 7.7$.[36] Moreover, our objectives are to analyze the Ravaché-Mountain-Streett (RMS) freezing criterion ratio,[15–17]

$$R_{RMS} = g_f(r_{dip})/g_f(r_m), \qquad (6)$$

in its dependence on λ, to characterize the isothermal compressibility factor, $S_f(q \to 0)$, along the freezing line, and to search for possible inter-relations of the characteristic distances related to $g_f(r)$ and $S_f(q)$ with those observed in the bcc and fcc phases near the triple point. We also examine the fluid-state mean number of next neighbors close to freezing for possible indications, if existing on level of the fluid-side structure factor and RDF, on whether the system freezes into a bcc or fcc solid, and we investigate the behavior of the pair potential $u(r)$ near freezing both for systems with low- and high λ values.

The present Paper II includes an elaborate extension of the accompanying earlier Paper I which contained also experimental results on charged silica spheres in DMF. Thus, as for Paper I, the present paper is addressing experimentalists and theoreticians alike. From a purely theoretical viewpoint, the discussion of the mean local microstructure at freezing could be entirely, and most conveniently, made in the framework of the two-dimensional $(\lambda, \tilde{T})$ phase space. However, experimentalist performing scattering or real-space imaging experiments do not have independent control of these two reduced parameters, and their respective influence on the microstructure at freezing is not as easily predictable than for the experimental control parameters. For this reason, and to maintain a strong link to Paper I even though no experimental results are included here, the discussion in the present paper is formulated partially in terms of experimental parameters characteristic for charged silica spheres dispersed in DMF. We note here that the concept of following a colloidal system property along lines in the $(\lambda, \tilde{T})$ phase space created by a single experimental parameter variation was used before in, e.g., Refs. 29 and 40. These lines are referred to by Liu et al.[40] as state lines, while in Papers I and II they are named trajectories.

An interesting finding in Paper I was that the application of the RY method in conjunction with the HV freezing rule gives complex freezing lines in terms of experimental parameters reducing all to a single freezing line in $(\lambda, \tilde{T})$ space which is overall in good agreement with the simulation predictions. Freezing line calculations using the simple RY-HV method are much faster than the ones by Molecular Dynamics (MD) or Monte Carlo (MC) simulations. The RY-HV method is thus a convenient and reliable tool for generating the various experimental freezing lines. Moreover, as we are going to show here, it can be profitably used for the theoretical exploration

of the behavior of various static properties along the $(\lambda, \tilde{T})$ freezing master curve. We explore in particular the height of the principal peak of $g(r)$ at freezing, characteristic lengths associated to $g(r)$ and $S(q)$, and the behavior of the particle coordination number and the isothermal osmotic compressibility factor.

The specific experimentally controllable system parameters employed in our RY-HV calculations represent suspensions of charge-stabilized monodisperse silica spheres in DMF with various amounts of lithium chloride added. Experimental results for these systems have been included in Paper I, and in another work by us.[10] We assume a constant temperature of $T = 293$ K, spherical particles of diameter $\sigma = 171$ nm, and DMF as solvent with dielectric constant $\varepsilon = 36.7$, corresponding to the Bjerrum length $L_B = e^2/(\varepsilon k_B T) = 1.55$ mm. Freezing lines in terms of pairs of the experimental control parameters ϕ, C_s, and Z have been calculated in Paper I using the RY integral equation method with a constant HV structure factor peak value $S_f(q_m) = 3.1$ used as the freezing transition indicator. In the present RY-HV calculations of $S(q)$ and $g(r)$ based on the same constant structure factor principal peak value, a vast range of experimental control parameters has been used corresponding to a $(\lambda, \tilde{T})$ freezing line extending far out to large λ values. The results presented here for the various structural properties at freezing are largely based on the elaborate RY-HV generated data base of static structure factors and RDFs employed already in Paper I.

In the Yukawa pair potential employed in the present study, the most delicate parameter is the effective particle charge number Z. In an operational way, it can be determined from matching the theoretical structure factor peak to the experimental one. However, the occurrence of low-charge and high-charge branches discussed in Paper I shows that this matching provides not necessarily a unique charge value. It is to a larger extent unexplored to date how the effective charge values determined from the measurement of different properties such as electrophoretic mobility, shear modulus, and structure factor principal peak are precisely interrelated. Experimental works on this issue include colloidal probe experiments with atomic force microscopy,[41] electrophoresis,[42,43] optical tweezers and microscopy experiments,[44] as well as conductivity measurements,[45] and torsional resonance spectroscopy.[46] Different effective charges have been compared by Shapran et al.[47] in a joint experimental-theoretical study. The effective charge characterizing a specific property is deduced in experiments on basis of a theoretical underpinning which to date is only approximate. It is still under debate how a property-related effective charge is quantitatively related to the so-called bare charge. This is referred to as the charge-renormalization (many-body) problem. The bare charge is defined on a more fundamental level of description where the microions are treated as separate entities. The effective colloid charge in relation to the bare one can be estimated using simplifying mean-field-type spherical cell model[48–50] and self-consistent jellium model calculations,[51,52] and non-mean-field generalizations accounting for non-monovalent microions[53] and finite microion sizes.[54] Noteworthy is a recent primitive model based HNC integral equation study

where also chemical charge regulation on the colloid surfaces has been considered.[55]

As in Paper I, we refrain from including charge renormalization into our quantitative analysis since it is out of the scope of the present general study where no specific experimental data are discussed. We merely point out here that the predicted value for the ratio of effective to bare colloid charge can vary significantly, depending on the invoked (approximate) charge renormalization method and chemical charge regulation scheme.

We further remark that in the analysis of scattering data, polydispersity in particle size and effective charge can be a source of serious misinterpretations of the actual interaction parameters, if polydispersity is not properly accounted for in the underlying theoretical modeling. For a discussion, see, e.g., Refs. 56 and 57. Polydispersity leads in particular to an enlarged forward scattering, with the consequence that the measured structure factor at small wavenumbers cannot be identified any more with the osmotic compressibility factor. Polydispersity has the additional effect of damping the wavenumber dependent undulations in the measured structure factor. While being usually troublesome, one can take advantage of a small amount of polydispersity in the determination of electrophoretic particle velocities.[58] In this paper dealing with generic static properties of Yukawa particle systems, we restrict ourselves to monodisperse spheres.

The paper is organized as follows: The results on our RY-HV study of the local microstructure at freezing are presented in Sec. II. In Subsections II A–II C, the general behavior of the reduced screening parameter, the Debye screening length, and pair potential are examined, for a large variety of systems with different amounts of added salt. This serves as a prerequisite for the subsequent discussion in Subsection II D of a variety of microstructural properties. A summary of the obtained results is included in Sec. III.

II. RESULTS AND DISCUSSION

A. Universal $\tilde{T}$-λ phase diagram

The universal freezing line of Yukawa-type colloidal particle systems with masked excluded volume interactions, as predicted by the RY-HV scheme and calculated in Paper I using the constant HV value $S_f(q_m) = 3.1$, is shown in Fig. 1 (colored symbols). The RY-HV predicted freezing line is seen to be in good overall agreement with previously published simulation results for the fluid-solid phase separation lines by Stevens and Robbins[34] and Hamaguchi *et al.*[35] The latter two separation lines are represented in the figure by the solid lines.

Note that the RY-HV freezing line for Yukawa systems with masked excluded volume interaction covers a broad range of λ values extending up to 60 (see the inset). In principle, the freezing line must be distinguished from the melting line located somewhat below the former one.[37] However, the difference is small for smaller values of λ, and the (density) difference vanishes altogether at the one-component plasma (OCP) limit $\lambda \to 0$ of zero electrostatic screening where $\tilde{T}_{OCP} = \tilde{T}_f(\lambda = 0) \approx 9.383 \times 10^{-3}$ corresponding to
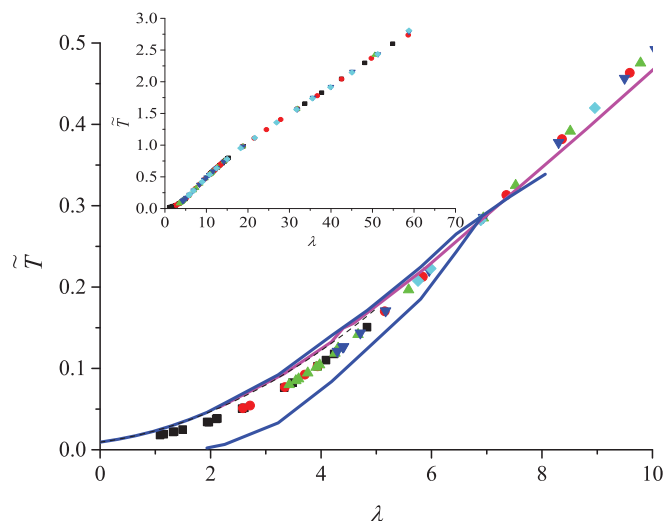

FIG. 1. $\tilde{T}$ vs. λ universal phase diagram of point-Yukawa particles. The freezing line obtained in Paper I using the RY-HV scheme with $S_f(q_m)$ = 3.1 (symbols) is compared with the simulation predictions by Hamaguchi *et al.*[35] (blue line) and Stevens and Robbins[34] (purple line). The dashed black line for $0 < \lambda < 5$ represents Eq. (7). It practically coincides with the predictions of Stevens and Robbins. The inset shows the RY-HV freezing line for an extended screening parameter range.[9] Different colors of the symbols correspond to the different iso-C_s lines, which cover a very broad range of values for ϕ and Z.

the coupling parameter $\Gamma_{OCP} = \Gamma_f(\lambda = 0) \approx 106$. As an illustration of this point, we refer to Figs. 9(a) and 9(b) in Paper I where both the melting and freezing line predictions by Stevens and Robbins[34] are shown. The coexistence regions in charge-stabilized systems have been studied also experimentally,[29,59,60] and in various cases the regions of coexistence were found to be quite extended. It should be noted here that the density difference in the coexisting fluid and solid phases is non-universal, being determined not only by the system specific concentration dependencies of the effective colloid charge and screening parameter but also by the microion degrees of freedom influencing the state-dependent free volume contribution to the free energy (see, e.g., Ref. 61). In this work, we are only concerned with the microstructure along the freezing line. The fluid-phase based RY-HV scheme does not allow to map out fluid-solid coexistence regions.

The employed constant HV $S_f(q_m) = 3.1$ is in agreement with our x-ray scattering experiments on coated silica spheres in DMF,[10] and conforms to computer simulation results[32,34] and density functional theory calculations[37,62] where for masked-core Yukawa particles HV freezing values around 3 have been reported. As noted already in Paper I, according to our calculations the universal freezing line in the $(\lambda, \tilde{T})$ phase space does not change significantly if the HV peak value is altered by ±0.1.

For smaller values, $\lambda \le 5$, of the reduced screening parameter, the freezing line obtained from computer simulations is well parameterized by[25]

$$\tilde{T}_f(\lambda) \approx \tilde{T}_{OCP}[1 + \lambda + \lambda^2/2]. \tag{7}$$

A characteristic feature of the universal phase diagram is the presence of a bcc phase space part at smaller values of λ and $\tilde{T}$. The HV criterion does not allow for distinguishing

the fluid-bcc transition that takes place for smaller screening parameters from the fluid-fcc transition at larger values of λ. The triple point of three-phase fluid-bcc-fcc coexistence, which bisects the freezing line into the lower λ and higher λ parts, is located according to Hamaguchi *et al.*[35] at $(\lambda_t = 6.90, \tilde{T}_t = 0.2856)$. In more recent simulation work by Hoy and Robbins,[36] a somewhat larger value of $\lambda_t = 7.7$ has been predicted for the reduced screening parameter at the universal freezing line triple point. Thus, to our knowledge, there is still some uncertainty about the precise location of the triple point. As for the fluid-solid and solid-solid coexistence regions, the RY-HV method does not allow to determine the triple point of three phases coexistence.

B. Dependence of λ on experimental control parameters

The interpretation of the universal $\tilde{T}$-λ phase diagram in Fig. 1 in terms of the experimentally controllable parameters is not straightforward. A charge-stabilized colloidal system is characterized by the following set of experimental control parameters: sphere radius $a = \sigma/2$, effective charge number Z, volume fraction ϕ, colloid number concentration n, added salt concentration C_S, and the dielectric constant, ε, of the solvent at a given temperature T. A given set of these parameters corresponds to a single value for λ and $u(\langle r \rangle)$, respectively. However, a specific value for λ can be realized by different combinations of experimental control parameters. This is exemplified in Fig. 2, where λ is plotted as a function of ϕ for systems at freezing having different salt concentrations.

According to the λ-ϕ freezing lines in Fig. 2, two different values of λ are found for each value of ϕ at a given salt concentration. These values form the low-charge (LZ, lower curve segments) and high-charge (HZ, upper curve segments) branches, respectively, of the iso-C_s freezing lines. As we

FIG. 3. Mean inter-particle distance $\langle r \rangle$ (black solid line), and iso-C_s freezing lines of the Debye screening length κ^{-1} (symbols), for the systems in Fig. 2, and in Fig. 7 of Paper I. Different colors mark different iso-C_s lines.

have discussed in detail in Paper I, for many systems of a given volume fraction and salt concentration, the same structure factor peak height is obtained in general for two very different effective charge values. The two structure factors are hard to distinguish from the viewpoint of experimental factors (true volume fraction, instrument resolution, background), which may lead to serious errors in positioning the experimental points on the universal phase diagram due to substantial differences in the λ values of the LZ and HZ solutions. For the systems at freezing studied in this work, the values of λ in the LZ branch cover the range from about 2 to 12 but values of λ mainly smaller than 7 are assumed. The values of λ in the HZ branch are larger than for the low-charge branch solutions, owing to the larger values that κ attains for high colloid effective charges. The HZ branch values of λ are all located within $8 < \lambda < 60$. For the majority of HZ systems, however, values in the more narrow range of $8 < \lambda < 15$ are observed.

Note from the figure that the same value for λ can be realized by systems at freezing for values for ϕ, C_s, and Z differing by several orders of magnitude. This can be understood from analyzing the dependence of the mean pair distance, $\langle r \rangle$, and the Debye screening length, κ^{-1}, on ϕ and C_s as depicted in Fig. 3. One sees from this figure that in going along a low-salt iso-C_s line, ϕ changes by 7 orders, $\langle r \rangle$ by 2 orders, and κ^{-1} by about 3 orders of magnitude.

The figure further reveals that at low and intermediate ϕ values, $\langle r \rangle$ and κ^{-1} decline roughly in parallel with increasing ϕ, giving rise to comparatively little changes in $\lambda = \langle r \rangle \kappa$. For the HZ branch at high ϕ, the decrease of the Debye screening length with increasing concentration is much stronger than the one of $\langle r \rangle$ which results in a strong increase of λ (Fig. 2). In Fig. 3, the upper part of each iso-C_s curve for κ^{-1} corresponds to the LZ, and the lower part to the HZ branch solutions for $S_f(q)$, as indicated in the figure. Note that the Debye screening length at freezing is always smaller than the geometric mean inter-particle distance.
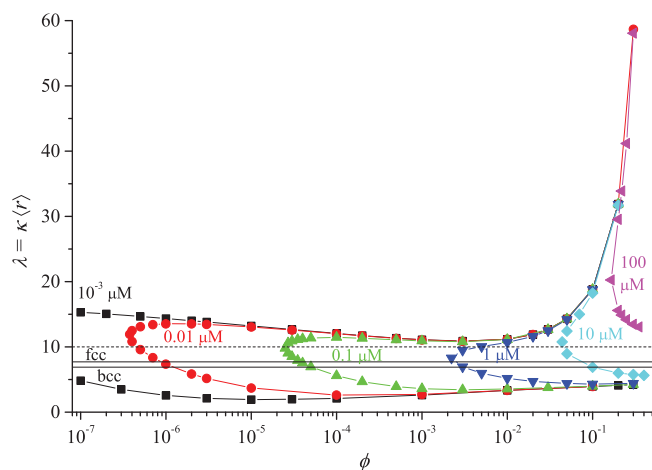
FIG. 2. Values of the reduced screening parameter $\lambda = \kappa \langle r \rangle$ for systems at freezing discussed in the associated $C_s - \phi$ freezing lines diagram in Fig. 7 of Paper I. The two solid horizontal lines at $\lambda = 6.9$ and $\lambda = 7.7$ mark the somewhat different simulation predictions for the fluid-bcc-fcc triple point value, λ_t, in Refs. 35 and 36, respectively. Different colors of the symbols correspond to different iso-C_s freezing lines, with the values for C_s indicated in the figure.
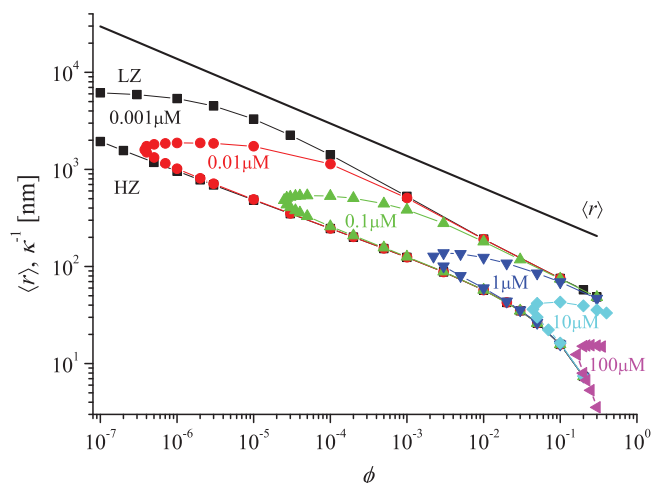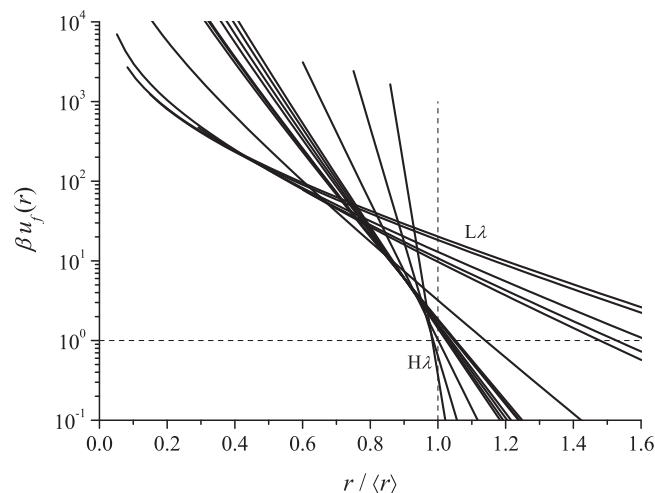
FIG. 4.   Reduced pair interaction energy $\beta u_f(r)$, at freezing calculated for different values of the screening parameter λ ranging from low-λ values (Lλ: $\lambda < \lambda_t$) to high-λ values (Hλ: $\lambda > \lambda_t$). The usage of the normalized distance parameter $r/\langle r \rangle$ reduces the freezing curves for a given λ to a single line (cf. Eq. (3)). The pair energy at mean particle distance, $\beta u_f(\langle r \rangle)$, has values covering two orders of magnitude, and it is smaller for the Hλ systems while for the Lλ systems it is larger.

C. Pair interaction energy at freezing

To examine the role of the pair interaction energy, $u(r)$, at freezing, in Fig. 4 we plot $u_f(r)/k_BT$ as a function of the reduced distance $r/\langle r \rangle$. A logarithmic scale is used for the displayed reduced pair energies covering several orders of magnitude. Depending on the specific system, the pair energy at mean distance, $u_f(\langle r \rangle)$, changes from about 0.5 k_BT to about 40 k_BT. In addition, the slope of $u_f(r/\langle r \rangle)/k_BT$, which in the present linear-log plot is equal to $-(\lambda + \langle r \rangle/r)/2.3$, covers a broad range of values for the considered reduced screening parameter range.

In Fig. 4, the subset of curves for systems where λ is small (labeled Lλ) in the sense that $\lambda < \lambda_t$, is qualitatively different from the subset of systems with $\lambda > \lambda_t$ large (labeled Hλ). The Lλ subset is entirely composed of LZ systems. In contrast, the Hλ subset consists both of HZ systems and a smaller fraction of LZ systems. The reduced pair energy at mean distance, $u_f(\langle r \rangle)/k_BT$, of the L$\lambda$ systems at freezing is large, with values from 5 to 40 k_BT, but the absolute value of the (negative) slope of the potential energy is quite small. Thus, the pair potential of Lλ systems is long-ranged.

Quite differently from this, the $u_f(\langle r \rangle)$ values of the Hλ systems at freezing are comparatively small, in the range from 0.5 to 5 k_BT, but the absolute value of the potential slope is much larger than that of the Lλ systems. The pair potential of Hλ systems decays rather steeply.

These general features of $u(r)$ are related to the freezing behavior: Lλ systems characterized by $\lambda < \lambda_t$ and a long-ranged $u(r)$ freeze into bcc crystals (see Fig. 1), whereas the Hλ systems characterized by $\lambda > \lambda_t$ and a short-ranged pair potential form fcc crystals at freezing.

The screening of the electrostatic pair interactions between colloidal spheres is caused both by counterions released from colloid surfaces and dissociated added salt ions. The square of the Debye screening parameter, $\kappa^2 = \kappa_{ci}^2$
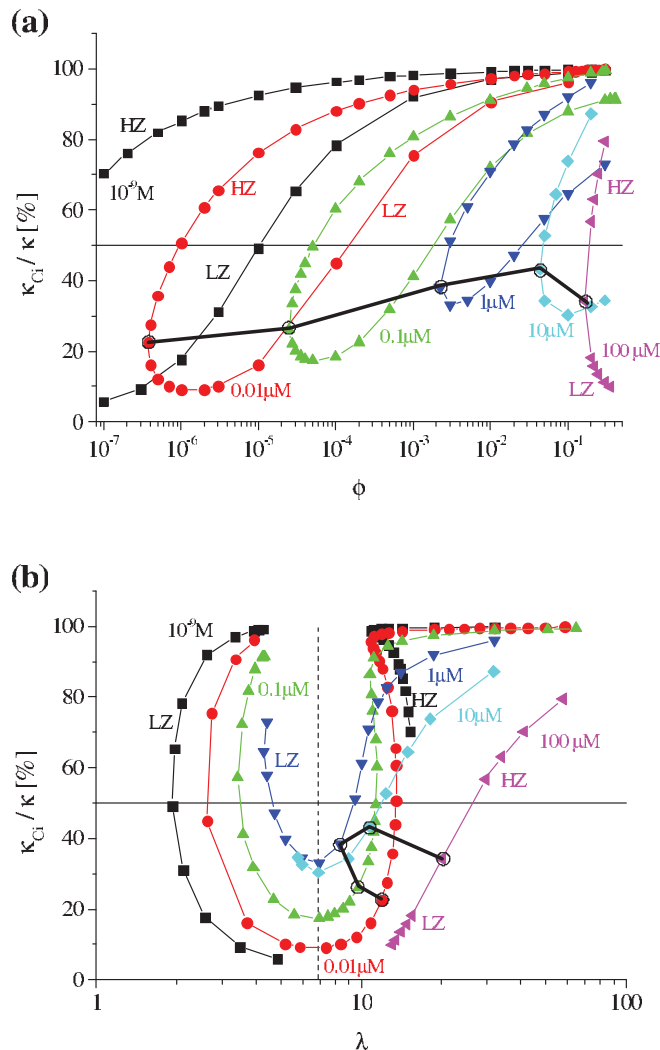
FIG. 5.   Relative contribution of surface-released counterions (ci) to the Debye screening parameter, κ, for the systems in Fig. 2, as a function of ϕ in (a) and λ in (b), respectively. LZ and HZ label the low-charge and the high-charge branch systems, respectively. The horizontal solid line marks $\kappa_s = \kappa_{ci}$. The thick black line connects systems separating the LZ and HZ branches along the considered iso-C_s lines, both in (a) and (b). The vertical dashed line in (b) indicates the triple point value λ_t of the fcc-bcc crossover at the freezing line. Different colors of the symbols correspond to the different iso-C_s freezing lines. The same color code as in Fig. 2 is used.

$+ \kappa_s^2$, consists thus of the surface-released counterion contribution, κ_{ci}^2, and the salt ion contribution κ_{Cs}^2. The set of screening parameter values for which $\kappa_s \approx \kappa_{ci}$ marks the transition regime from surface counterion to salt ion dominated microstructure.

The ratio, κ_{ci}/κ, of surface-released counterions to the total screening parameter is shown in Figs. 5(a) and 5(b) as a function of ϕ and λ, respectively, for systems at freezing covering a broad range of colloid and salt concentrations. From this figure, one directly identifies the regions where the screening parameter is dominated either by surface-released counterions or added salt ions. Note that these regions are not directly correlated with the LZ and HZ branches.

In Fig. 5(a), each iso-C_s curve has a point of smallest volume fraction ϕ for which a system can crystallize according to the RY-HV rule. These points are connected in the figure by thick black solid line segments, and they separate along each

iso-C_s line the LZ from the HZ systems (as indicated in the figure). From Fig. 5(a), one notices that all these points are located in the salt dominated region where $\kappa_s > \kappa_{ci}$.

Fig. 5(b) depicts the iso-C_s lines for κ_{ci}/κ as functions of the reduced screening parameter. Quite interestingly, on increasing the colloid concentration along the LZ branch of each iso-C_s curve for κ_{ci}/κ, a minimum of all curves at about the same value $\lambda \approx 6.9 \approx \lambda_t$ is observed, followed by a rapid increase towards the counterion dominated region at high colloid concentrations. The minima in Fig. 5(b) at $\lambda \approx \lambda_t$ correspond to the minima in Fig. 5(a). The latter are however dispersed over five orders of magnitude in the volume fraction. At first sight, the concave shapes of the iso-C_s curves in Fig. 5(b) with a minimum at $\lambda \approx \lambda_t$ appear surprising, since with increasing ϕ more counterions should be present and hence κ_{ci}/κ should become larger (assuming a constant Z). However, on moving along a freezing line each point in the line represents a system with its own specific effective charge. And indeed, the effect of increasing ϕ starting from very low concentration is more than compensated by an accompanying decrease in Z so that κ_{ci}/κ is decreasing until the minimum at $\lambda \approx \lambda_t$ is reached. When ϕ is further enlarged, the counterion contribution to screening increases monotonically. Not only the relative contribution of κ_{ci} to κ has a minimum at $\lambda \approx \lambda_t$. Also in absolute numbers κ_{ci} has a minimum for the same value of λ. Moreover, since along the iso-C_s line $\kappa_s = $ const, the total screening parameter κ has as well a maximum at this point. Fig. 5 suggests that along each iso-C_s freezing line the Debye screening length is largest at $\lambda \approx \lambda_t$.

Note finally that the complicated looking shape of the curves in Fig. 5(b) is a consequence of the non-monotonic volume fraction dependence of λ.

D. Microstructure at freezing and related lengths

1. Static structure factor and radial distribution function

Information on the radially averaged near-range ordering of an isotropic colloidal fluid is encoded in the equilibrium RDF $g(r)$ through its dependence on the distance, r, between pairs of colloidal spheres. The same microstructural information, but encoded now in the reciprocal wavenumber space, is included in its inverse Fourier transform pair, the static structure factor $S(q)$. The latter quantity is more easily accessible experimentally in a three-dimensional bulk suspension by using scattering experiments. The fluid microstructure, on the other hand, is best analyzed theoretically in real space in terms of $g(r)$. Both in experiments and computer simulations, $g(r)$ and $S(q)$ can be obtained accurately only in a limited range of r and q values, respectively. On the other hand, integral equation schemes such as the RY method allow for the calculation of these functions over extended ranges of their arguments.

In Figs. 6(a) and 6(b), the RY-HV calculated Fourier transform pairs, $S_f(q)$ and $g_f(r)$, fulfilling the HV freezing
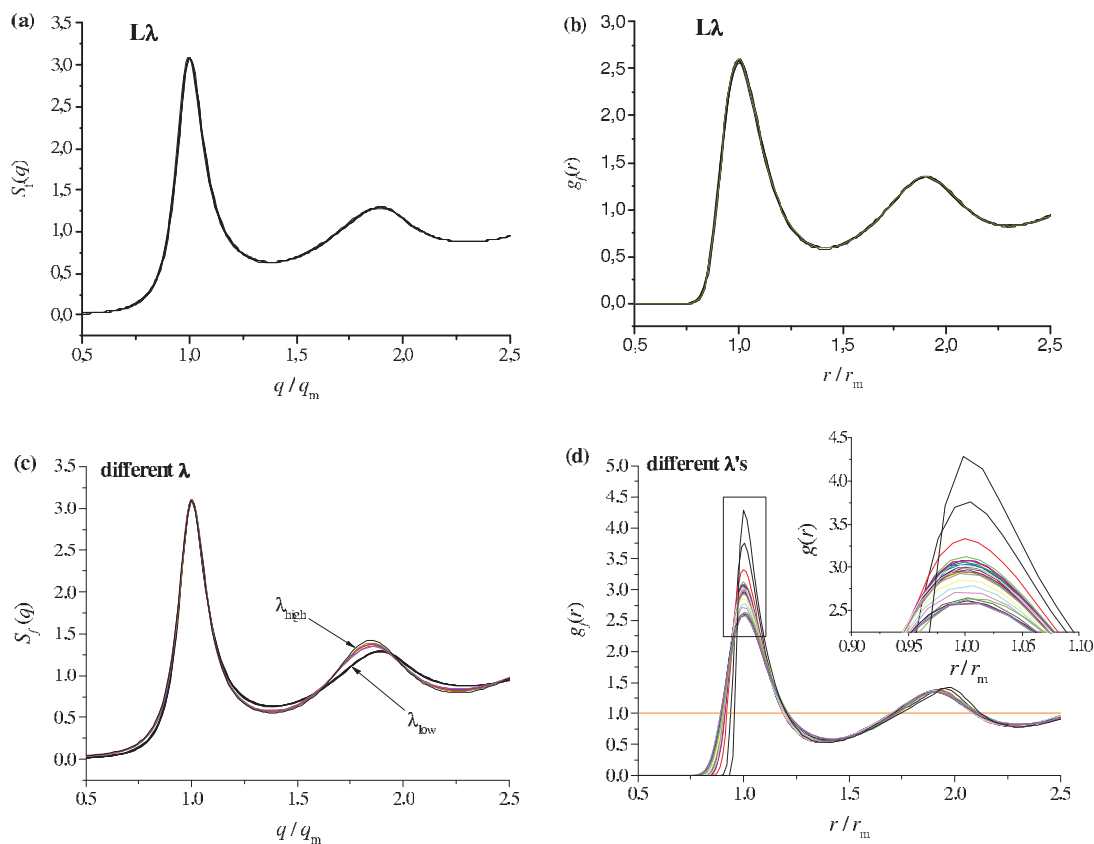
FIG. 6. RY-HV predicted static structure factors and RDFs at freezing, for Lλ systems where $\lambda < 6.9 \approx \lambda_t$ (in (a) and (b)), and systems covering a broad range of λ values from 2 to 60 (in (c) and (d)). The inset in (d) magnifies the principal peak region of $g_f(r)$. Pair distance and wavenumber are scaled in units of the principal peak positions r_m and q_m of $g_f(r)$ and $S_f(q)$, respectively. Note that the respective $S_f(q)$'s and $g_f(r)$'s of the Lλ systems nearly coincide, whereas the systems in (c) and (d) vary significantly regarding the RDF peak height.

FIG. 7. RY-HV predicted principal peak height of the RDF at freezing, plotted as a function of λ (symbols). The two vertical dashed lines indicate the fluid-bcc-fcc triple point values $\lambda_t = 6.9$ and 7.7 according to the simulation predictions by Hamaguchi *et al.*[35] and Hoy and Robbins,[36] respectively. The inset depicts the peak height as a function of ϕ, for various added salt concentrations. Different colors of the symbols distinguish different iso-C_s freezing lines. The dotted line in the inset separates the LZ branch (lower part of curves) from the HZ branch (upper part of curves).

FIG. 8. RY-HV mixing function, $f(\alpha r_m)$, at freezing as a function of λ.

criterion of peak height 3.1 are shown for a variety of Lλ systems with $\lambda < 6.9 \approx \lambda_t$. The wavenumber q and pair distance r are scaled in units of the positions, q_m and r_m, of the principal peaks of S_f and g_f, respectively. Quite interestingly, the structure factors and RDFs of all depicted Lλ systems are practically coincident even though the volume fraction, with $10^{-7} < \phi < 0.3$, and the added salt concentration, with 10^{-3} μM $< C_s < 10$ μM, vary by several orders of magnitude (see also Fig. 2). While the structure factor peak height, $S_f(q_m) = 3.1$, is fixed by the employed HV condition, also the RDF peak height is practically constant with value $g_f(r_m) \approx 2.6$. Note that the effective temperature of the considered Lλ systems is not constant but varies by one order of magnitude in the interval $0.03 < \tilde{T} < 0.3$, as it can be noticed from Fig. 1.

In Figs. 6(c) and 6(d), $S_f(q)$ and $g_f(r)$ are depicted for a broad range, $2 \leq \lambda \leq 60$, of reduced screening parameter values extending up to large values. For the Hλ systems where $\lambda > \lambda_t$, the Fourier transform pairs change visibly with increasing λ. This changes are most pronounced in the principal peak region of the RDF, with $g_f(r_m)$, increasing from 2.6 to 4.3, for λ increasing from λ_t to 60. The RDF peak height for the largest considered screening parameter $\lambda = 60$ is still well below the value, $g_f^{HS}(r = \sigma^+) \approx 5.81$, of the RDF peak height of a neutral hard-sphere system at the freezing volume fraction $\phi_f^{HS} \approx 0.49$, for the reason that charge-stabilized spheres with zero contact probability are considered in this work. The RDF of neutral hard spheres, on the other hand, has its maximum at the contact distance $r = r_m = \sigma$.

To analyze $g_f(r_m)$ in more detail, in Fig. 7 we plot the RDF peak height as a function of λ (main figure) and ϕ (inset). We first notice from the inset that the shapes of the iso-C_s freezing lines resemble those in Fig. 2. The different iso-C_s lines in the inset add up to a single freezing line for $g_f(r_m)$ plotted as a function of λ. The various iso-C_s contributions to this universal line for $g_f(r_m)$ versus λ are visible in Fig. 7

by their different colors. The RDF peak height at freezing is practically constant with value $g_f(r_m) \approx 2.6$, for $\lambda < 5$, which is close to λ_t. For larger screening parameters, $g_f(r_m)$ increases monotonically.

Recall on viewing Fig. 1 that at freezing there is a one-to-one relation between λ and $\beta u_f(\langle r \rangle) = 1/\tilde{T}$. A relation between $g_f(r_m)$ and the reduced pair potential, $\beta u(r_m)$, at position r_m is provided by the RY closure relation,[11]

$$g(r_m) \approx e^{-\beta u(r_m)} + \frac{e^{-\beta u(r_m)}}{f(\sigma r_m)} \{ e^{f(\alpha r_m)[h(r_m) - c(r_m)]} - 1 \}, \quad (8)$$

where $f(\alpha r) = 1 - \exp[-\alpha r]$ is the RY mixing function, and $h(r) = g(r) - 1$ and $c(r)$ are the total and direct correlation functions, respectively. The mixing parameter value $\alpha \in \{0, \infty\}$ is determined self-consistently, for each set of system parameters, from enforcing the equality of the isothermal compressibility derived, respectively, from the pressure and compressibility equations of state. Fig. 8 shows the calculated RY-HV mixing function values at freezing. For small λ values, $f(\alpha r_m)$ is rather close to one, i.e., located near the limiting hypernetted-chain (HNC) side of the RY hybrid closure, while for large λ the Percus-Yevick (PY) limiting form of the RY closure is favored.

In Fig. 9, the two additive contributions to the RY-HV peak value $g(r_m)$ on the right-hand-side of Eq. (8) are separately shown. According to the figure, the practically constant peak height $g_f(r_m) \approx 2.6$ for $\lambda < \lambda_t$ is due to the second term in Eq. (8). The first contribution to $g(r_m)$ equal to the zero-concentration limit $\exp\{-\beta u(r_m)\}$ is practically zero for Lλ systems, for the reason that $\beta u(\langle r \rangle)$ is here large as compared to one, with $u(r_m) \approx u(\langle r \rangle)$ (see Fig. 4). Different from this, the monotonic increase of $g_f(r_m)$ for values $\lambda > \lambda_t$ is due to both terms in Eq. (8). Note here again in relation to Fig. 4 that $\beta u_f(\langle r \rangle) \approx 1$ for the Hλ systems where $\lambda > \lambda_t$.

We proceed by discussing the implications of the RY-HV freezing rule, for constant $S_f(q_m) = 3.1$, on the RMS freezing criterion ratio $R_{RMS} = g_f(r_{dip})/g_f(r_m)$ in Eq. (6) between the first minimum, $g_f(r_{dip})$, of the RDF at position $r = r_{dip}$ to the right of the principal peak region and $g_f(r_m)$. For particles interacting by a repulsive inverse-power-law potential
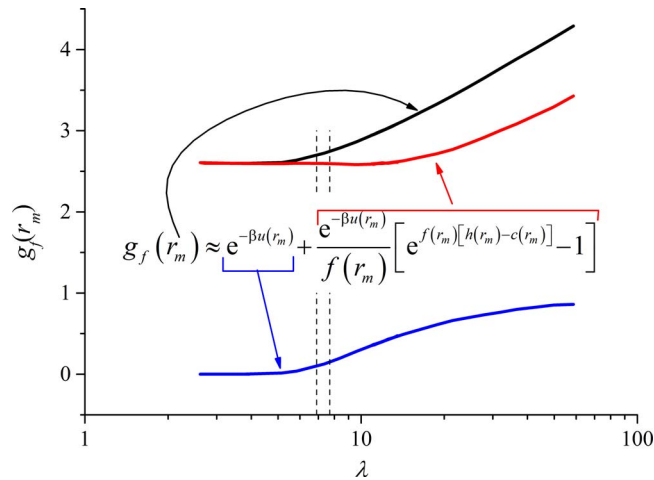
FIG. 9. RDF peak height contribution by the first term (lower solid blue curve) and second term (upper solid red curve) of the right-hand-side of Eq. (8) to $g_f(r_\mathrm{m})$ (solid black line). The dashed vertical lines at $\lambda_t = 6.9$ and $\lambda_t = 7.7$ mark the triple point predictions for λ_t in Refs. 35 and 36, respectively.

proportional to $1/r^n$, Hansen and Schiff[16] found in their MC simulations that at crystallization, R_{RMS} decreases from 0.26 at $n = 1$ to 0.1 at $n = 12$. The latter value is close to the RMS ratio for a neutral hard-sphere (HS) system at freezing.

Fig. 10 includes our RY-HV predictions for the RMS ratio as a function of λ. The RMS ratio is approximately constant for $\lambda \leq 5$, akin to $g_f(r_m)$ as depicted in Fig. 7, while for larger λ values the ratio decreases monotonically. In fact, the λ-dependence of R_{RMS} in Fig. 10 reflects essentially the λ-dependence of $g_f(r_m)$, since $g_f(r_{dip})$ changes only little, from 0.59 at small λ to 0.53 for the largest considered value $\lambda = 60$.

For small λ, the RY-HV scheme predicts $R_{RMS} \approx 0.23$ at freezing. This value is somewhat smaller than the value, $R_{RMS} = 0.26$, found by Hansen and Schiff[16] in the OCP limit, $\lambda \rightarrow 0$, of zero electric screening where they calculated $g_{OCP}(r_m) \approx 2.31$ and $g_{OCP}(r_d) \approx 0.61$. These two RDF values are very likely somewhat imprecise. In a recent HNC
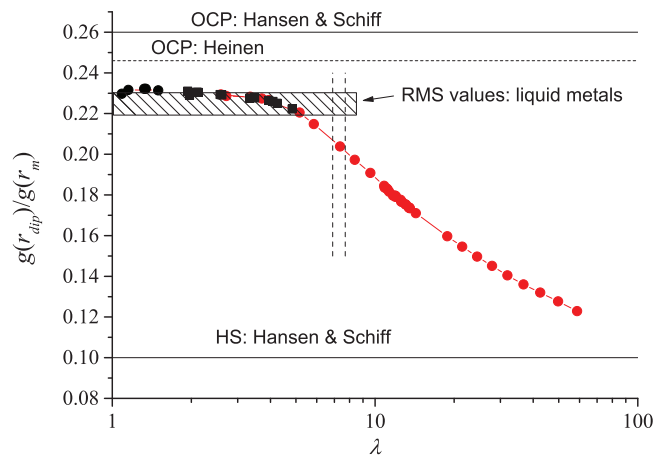
FIG. 10. RY-HV prediction for the ratio $R_{RMS} = g(r_{dip})/g(r_m)$ of point-Yukawa particles at freezing, as a function of λ. The dashed vertical lines at $\lambda_t = 6.9$ and $\lambda_t = 7.7$ are the triple point predictions in Refs. 35 and 36, respectively.

calculation by Heinen based on Ref. 63, the value $R_{RMS} \approx 0.246$ has been obtained for $\lambda \approx 0$ close to our RY-HV result. Quite interestingly, the R_{RMS} values measured in small angle X-ray and neutron scattering experiments on liquid metals in the vicinity of freezing are all located in a small interval next to 0.23 (see Fig. 10).[64, 65] We close the present discussion of the RMS ratio by pointing out that it is used in the literature not only as an indicator for crystallization. Wendt and Abraham have argued that $R_{RMS} = 0.14$ signals the transition into a supercooled liquid or amorphous state.[17]

2. Characteristic lengths

The RY-HV scheme provides in particular the values of the principal peak locations r_m and q_m of the RDF and static structure factor at freezing. We relate in the following these parameters to lengths and associated wavenumbers characterizing ideal and finite temperature colloidal fcc and bcc crystals of equal particle concentration.

For an ideal (i.e., zero temperature) fcc and bcc lattice, the distances $r_{m(i)}$ of the first three neighbor shells ($i = 1, 2, 3$) to a given particle are

$$a_{fcc}\frac{\sqrt{2}}{2}, \quad a_{fcc}, \quad a_{fcc}\sqrt{3/2} \quad \text{for fcc}, \tag{9a}$$

$$a_{bcc}\frac{\sqrt{3}}{2}, \quad a_{bcc}, \quad a_{bcc}\sqrt{2} \quad \text{for bcc}, \tag{9b}$$

where a_{fcc} and a_{bcc} are the edge lengths of the conventional fcc and bcc unit cells, respectively.

Using the relations between a_{fcc}, a_{bcc} and the mean interparticle distance $\langle r \rangle = n^{-1/3}$ given by

$$a_{fcc} = \sqrt[3]{4}\langle r \rangle \approx 1.5874\langle r \rangle, \tag{10a}$$

$$a_{bcc} = \sqrt[3]{2}\langle r \rangle \approx 1.2599\langle r \rangle, \tag{10b}$$

we can re-express the distances in Eq. (9) in units of $\langle r \rangle$ as

$$2^{1/6} \approx 1.122\,(12), \quad 2^{2/3} \approx 1.587\,(6),$$
$$2^{1/6}3^{1/2} \approx 1.944\,(24) \quad \text{for fcc}, \tag{11a}$$

$$2^{-2/3}3^{1/2} \approx 1.091\,(8), \quad 2^{1/3} \approx 1.260\,(6),$$
$$2^{5/6} \approx 1.782\,(12) \quad \text{for bcc}. \tag{11b}$$

The numbers in parentheses give the numbers of neighbors for the considered nearest neighbor distances.

The wavenumbers $q_{m(i)}$ of the first three Bragg peaks for both zero-temperature lattices are accordingly

$$\frac{2\pi}{a_{fcc}}\sqrt{3}, \quad \frac{2\pi}{a_{fcc}}\sqrt{4}, \quad \frac{2\pi}{a_{fcc}}\sqrt{8} \quad \text{for fcc}, \tag{12a}$$

$$\frac{2\pi}{a_{bcc}}\sqrt{2}, \quad \frac{2\pi}{a_{bcc}}\sqrt{4}, \quad \frac{2\pi}{a_{bcc}}\sqrt{6} \quad \text{for bcc}. \tag{12b}$$

Using Eq. (10), the first three Bragg peak wavenumber positions expressed in units of $2\pi/\langle r \rangle$ are

$$2^{-2/3}3^{1/2} \approx 1.091, \quad 2^{1/3} \approx 1.260, \quad 2^{5/6} \approx 1.782 \quad \text{(fcc)},$$
(13a)

$$2^{1/6} \approx 1.122, \quad 2^{2/3} \approx 1.587, \quad 2^{1/6}3^{1/2} \approx 1.944 \quad \text{(bcc)}.$$
(13b)

From this it follows for the first Bragg peak wavenumbers of the fcc and bcc lattice that $\frac{2\pi}{\langle r \rangle q_m^{fcc}} = 0.917$ and $\frac{2\pi}{\langle r \rangle q_m^{bcc(1)}} = 0.891$, respectively.

Using Molecular Dynamics (MD) simulations, Robbins *et al.*[31] presented orientationally averaged RDF $g(r)$ for the fluid and bcc and fcc crystalline phases of point-Yukawa systems with small ($\lambda \approx 3$) and moderately large ($\lambda \approx 10$) values of the reduced screening parameter. Different from an ideal infinite crystal where only sharp peaks (spikes) are present, for the simulated high-temperature crystals they found substantial thermal broadening of the RDF peaks. In the case of the high-temperature bcc solid ($\lambda \approx 3$) the first two zero-temperature spikes at relative distance 1.091 and 1.260 have merged into a single broadened next-neighbor peak of $g(r)$ having a slight shoulder. In their analysis of the number of nearest neighbors on basis of $g(r)$, Robbins *et al.*[31] treat this peak accordingly as a single layer. One can roughly estimate the average position of this merged particle layer by the population-averaged mean position, $r_{bbc(2)}$, of the first two neighboring bcc lattice spikes (cf. Eq. (11b)) according to

$$r_{bcc(2)}/\langle r \rangle = (8 \times 1.091 + 6 \times 1.260)/(8+6) = 1.163.$$
(14)

For the upcoming analysis of the RY-HV pair functions at freezing, we summarize the ideal-crystal based lengths,

$$r_{fcc} = 1.122\langle r \rangle,$$
$$r_{bcc} = 1.091\langle r \rangle,$$
$$r_{bcc(2)} = 1.163\langle r \rangle,$$
$$\frac{2\pi}{q_m^{fcc}} = 0.916\langle r \rangle,$$
$$\frac{2\pi}{q_m^{bcc}} = 0.891\langle r \rangle,$$

characterizing the next-neighbor layer of an ideal macroscopic fcc and bcc solid.

In place of $r_{bbc(2)}$, a more useful general definition of the mean next-neighbor distance suitable also for the high-temperature fcc solid and the fluid phase is given by

$$r_n = \frac{\int_0^{r_{dip}} r \cdot r^2 g(r) dr}{\int_0^{r_{dip}} r^2 g(r) dr},$$
(15)

where r_{dip} is the first minimum of $g(r)$ to the right of the (possibly merged) next-neighbor peak.

For comparison with our RY-HV predictions, we apply this definition to the MD-generated bcc and fcc RDFs by Robbins *et al.*[31] in their Figs. 14(a) (curve a) and 15(b) (curve a), respectively. The values for r_n calculated from their digi-
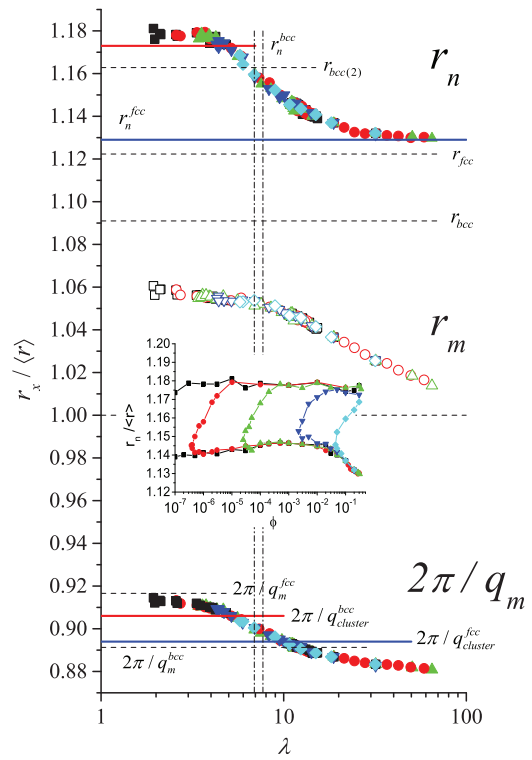

FIG. 11. Symbols: RY-HV predictions for mean next-neighbor distance r_n (top curve), the RDF peak position r_m (middle curve), and inverse structure factor peak position $2\pi/q_m$ (bottom curve) at freezing, plotted as functions of λ. All displayed lengths are in units of $\langle r \rangle$. The horizontal solid and dashed lines (with distinguishing labels) mark the characteristic lengths for a bcc and fcc solid discussed in the text. Dashed lines characterize ideal infinite bcc and fcc crystals, while the solid lines are derived from the simulations of small clusters. The inset shows the RY-HV values for r_n as a function of the volume fraction. The two vertical dashed-dotted lines mark the two predictions for the bcc-fcc crossover triple point. Different colors of the symbols correspond to the different iso-C_s freezing lines.

itized RDFs are $r_n^{fcc} = 1.129\langle r \rangle$ for the fcc ($\lambda = 10.1$) and $r_n^{bcc} = 1.173\langle r \rangle$ for the bcc solid ($\lambda = 3.19$).

While in Ref. 31 no orientationally averaged fcc-crystal structure factors $S(q)$ for larger λ values are shown, it can be expected that at the onset of crystallization the translational order is limited to a few unit cells and the first two closely spaced fcc Bragg spikes (see Eq. (13a)) are naturally broadened into a single principal peak. This expectation is supported by our numerical calculation of the orientationally averaged scattering intensity from small clusters of approximately 300 beads arranged in the ideal fcc (and bcc) structure. The wavenumber positions of the structure factor principal peak of the small fcc and bcc clusters are $q_{cluster}^{fcc}/(2\pi) = 1.118\langle r \rangle$ and $q_{cluster}^{bcc}/(2\pi) = 1.104\langle r \rangle$, respectively. Different from the infinite crystal case, the fcc cluster peak is located here to the right of the bcc peak, owing to the finite size effects and merging of the first two fcc Bragg peaks.

Fig. 11 summarizes the RY-HV freezing predictions for the characteristic lengths, r_n, r_m, and $(2\pi/q_m)$ in their dependence on λ. For comparison, the lengths r_{fcc}, r_{bcc}, $r_{bcc(2)}$, $2\pi/q_m^{fcc}$, and $2\pi/q_m^{bcc}$, characterizing the next neighbor and first Bragg peak positions of the ideal bcc and fcc lattice are depicted (with labels) as horizontal dashed lines. In addition, the lengths r_n^{fcc}, r_n^{bcc}, $2\pi/q_{cluster}^{fcc}$, and $2\pi/q_{cluster}^{bcc}$

characterizing a finite-temperature crystalline solid or cluster are depicted as solid horizontal lines (red for bcc and blue for fcc). The inset shows the ϕ-dependence of the RY-HV prediction for r_n.

We discuss now the content of this figure in progressing from top to bottom. The RY-HV curve for the mean distance, r_n, to the next neighbour shell describes a smooth monotonic decline from a low-λ plateau value (for $\lambda < 3$) corresponding to a bcc solid at freezing, to a smaller high-λ plateau value (for $\lambda > 30$) corresponding to a fcc solid at freezing. The predicted two plateau values obtained on basis of the fluid-phase HV criterion agree nicely with the values r_n^{fcc} and r_n^{bcc} (solid lines) for r_n gained from the digitized $g(r)$'s by Robbins *et al.* for thermally broadened fcc and bcc solids, respectively. A decent estimate of the bcc and fcc plateau values of the RY-HV r_n is obtained from using ideal crystal next neighbor distances only when r_{bcc} is replaced by $r_{bcc(2)}$. The latter length defined in Eq. (14) accounts approximately for the high-temperature merging of the first and second neighbour spikes into an effective first neighbour peak of $g(r)$.

Different from r_n, the principal peak position r_m of the fluid-phase RY-HV $g(r)$ at freezing is not a proper measure of the mean radius of the nearest neighbour shell in relation to the lengths characterizing the first neighbour shell of an ideal or high-temperature bcc and fcc solid. This is reflected in the middle part of Fig. 11 depicting values of r_m well below those for the crystal lengths.

The bottom part of the figure includes the RY-HV predictions for the inverse structure factor peak position ($2\pi/q_m$). At small $\lambda < 3$ and large $\lambda > 60$, two plateau values are approached whose values are very roughly described by the values $2\pi/q_{cluster}^{fcc}$ and $2\pi/q_{cluster}^{bcc}$ for a fcc and bcc ordered cluster, respectively. The difference can be attributed at least partially to the fact that the clusters are made of a few unit cells only. This results in a severe broadening of the bcc and fcc cluster structure factor peaks in comparison to the ones for an infinite crystal, and to a slight shift of the peak positions towards smaller q values. As discussed earlier, the first two Bragg spikes of the zero-temperature fcc cluster merge into a single effective structure factor peak located now to the right of the first peak of the bcc cluster. This explains the ordering $2\pi/q_{cluster}^{fcc} < 2\pi/q_{cluster}^{bcc}$ in the figure.

3. Number of nearest neighbors

As proposed by Robbins *et al.*,[31] the number of nearest neighbors N_n can be used as a probe of symmetry type in highly ordered colloidal suspensions. The mean number of nearest neighbors surrounding each particle can be expressed as

$$N_n = N(x_s = r_{dip}/\langle r\rangle), \qquad (16)$$

where

$$N(x_s) = \int_0^{x_s} 4\pi x^2 g(x)dx, \quad x = r/\langle r\rangle \qquad (17)$$

is the mean number of neighbors in a sphere of radius $r_s = x_s \cdot \langle r\rangle$, comparable to r_{dip}.
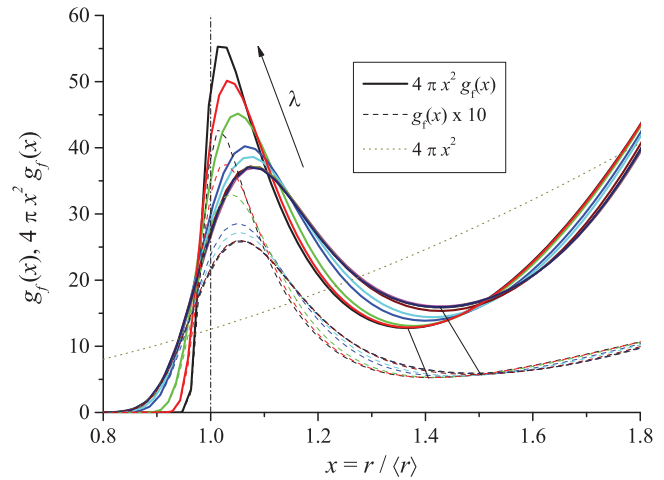

FIG. 12. RY-HV predictions of the radial dependencies of the three indicated quantities entering into Eq. (16). The radial distance is scaled in units of $\langle r\rangle$. Results for different values of λ are shown in the range from 1.93 to 58.7. The values for the RDFs $g_f(x)$ at freezing have been multiplied by the factor 10 for better visibility. The two inclined thin lines connect respective minima for the largest and smallest considered λ values (see text).

Here r_{dip} is the first minimum of $g(r)$ located to the right of its first peak. The number N_n is an indicator of the local ordering in a fluid or solid, with $g(r)$ in the latter case taken as the orientationally averaged pair distribution function. Since the first two shells of a high-temperature bcc solid form effectively a single layer, one finds $N_n(bcc) = 14$ according to Eq. (11a). The second particle shell of a fcc solid is well separated from the first one even in the high temperature regime so that $N_n(bcc) = 12$ holds as for the ideal crystal. According to Robbins *et al.*,[31] values of N_n close to 14 and 12 are thus indicative of a local bcc and fcc symmetry, respectively.

To explore the predictions of the RY-HV scheme for N_n, ten systems at freezing with different λ values in the range from 1.93 to 58.7 are considered in Fig. 12. The figure includes the respective $g_f(x)$ (multiplied by 10 for better visibility) and the integrand $4\pi x^2 g_f(x)$ going into the definition of the mean number of next neighbours. The radial distance is scaled by $\langle r\rangle$. We recall here with Fig. 7 that the principal peak of $g_f(x)$ is practically constant with value 2.6 up to $\lambda \approx 5$, from which it increases monotonically with further increasing λ up to 4.28 at $\lambda = 58.7$. The first peak of $4\pi x^2 g_f(x)$ is shifted to the right and the first minimum to the left relative to the corresponding maximum and minimum of the RDF, which obviously is due to the $4\pi x^2$ factor (dotted line in Fig. 12).

The function $N(x_s)$ for the considered ten RY-HV systems at freezing is displayed in Fig. 13. The location of the point of minimal slope (inflection point) of $N(x_s)$ coincides with the first minimum of $4\pi x^2 g(x)$ located, according to Fig. 12, to the left of the first minimum $x_{dip} = r_{dip}/\langle r\rangle$ of $g(x)$.

The mean number of next neighbors, N_n, as a function λ, obtained from Fig. 13 using its definition in Eq. (16) is shown in Fig. 14. For small λ values N_n, is rather close to $N_n(bcc_2) = 14$, suggesting that the colloidal fluid near freezing has for low λ a near-distance ordering resembling that of a high-temperature bcc crystal. With increasing λ, the number of nearest neighbors decreases slightly below N_n (fcc) = 12 which is typical of a fcc solid. The present results based on
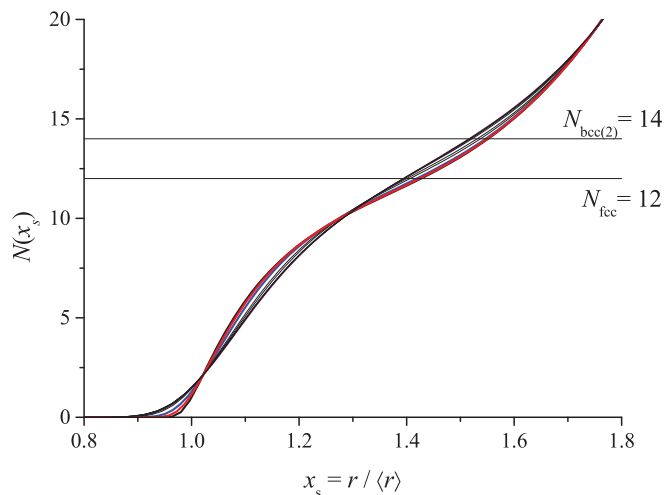
FIG. 13. Mean number of neighbors, $N(x_s)$ in a sphere of radius $r_s = x_s \langle r \rangle$ obtained using Eq. (17) from the RY-HV based RDFs at freezing shown in Fig. 10.

the RY-HV scheme should be contrasted with the corresponding MD simulation based findings by Robbins *et al.*[31] who find bcc-like local structure for their fluid-like $g(r)$'s even for $\lambda = 10.1$, with N_n close to 13.5. It should be noticed here that in Ref. 31, the inflection point of $N(x_s)$ is claimed to be used as the integration cutoff variable in Eq. (16) for N_n instead of x_{dip}. However, it is actually the positions of the minima of $g(r)$ shown in different figures of Ref. 31, that provide the N_n values reported by the authors (read from the plots of $N(x_s)$ or calculated from the digitized RDFs). We mention this because Ref. 31 is a well-established reference in the discussion of the local order of Yukawa colloidal systems.

The consequences of using the inflection point as the cutoff integration value is shown in Fig. 14, where the open symbols represent the RY-HV results for N_n obtained in that way. The difference is substantial and the latter values are incom-
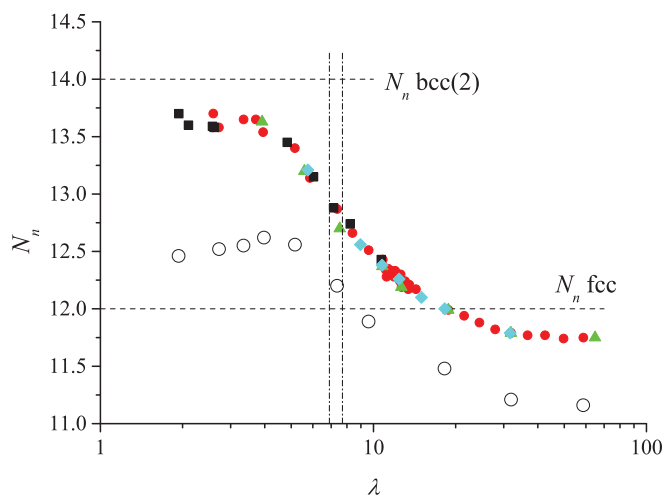

FIG. 14. Filled symbols: Mean number of next neighbors, N_n, for the RY-HV systems at freezing in Figs. 12 and 13. Different colors correspond to different iso-C_s freezing lines. The dashed vertical lines at $\lambda = 6.9$ and $\lambda = 7.7$ are the triple point predictions in Refs. 35 and 36, respectively. Open symbols: Values for N_n obtained if in place of r_{dip} the first minimum of $4\pi r^2 g(r)$ is used in Eq. (16).
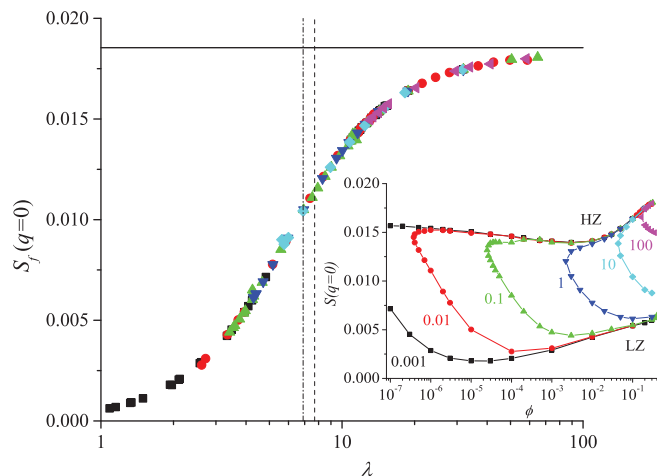

FIG. 15. Zero wavenumber limit, $S_f(q = 0)$, of the RY-HV static structure factor at freezing as a function of λ and ϕ (inset). The horizontal line at 0.01854 represents the RY result $S_f(q = 0)$ for neutral hard spheres at freezing ($\phi = 0.494$), compatible with the result from Carnahan-Starling model (0.01857). Different colors correspond to the different iso-C_s freezing lines of salt concentrations (in μM) indicated in the inset. The dashed vertical lines at $\lambda = 6.9$ and $\lambda = 7.7$ are the triple point predictions in Refs. 35 and 36, respectively.

patible with the former interpretation in terms of a bcc-like local structure at small λ and a fcc-like structure for large λ.

4. Isothermal osmotic compressibility

The isothermal osmotic compressibility, χ_T, of a one component colloidal system is given by

$$\frac{\chi_T}{\chi_T^{id}} = \lim_{q \to 0} S(q) = 1 + n \int d^3r(g(r) - 1), \qquad (18)$$

where $\chi_T^{id} = (nk_BT)^{-1}$ is the compressibility of an ideal gas.

In Fig. 15 the values of the structure factor extrapolated to zero q, i.e., $S_f(q = 0)$, at freezing are plotted vs. ϕ and λ, respectively, for colloidal systems of different charge, salt, and colloid concentrations.

While $S_f(q = 0)$ considered as a function of ϕ has a rather complex shape (see inset in Fig. 15), $S_f(q = 0)$ is a unique function of λ in accord with the discussion made in relation with Eq. (5). As expected, $S_f(q = 0)$ increases monotonically with increasing reduced screening parameter, since the pair potential becomes increasingly short ranged. In the $S_f(q = 0)$ versus ϕ diagram, the upper part of the curves corresponds to the high-charge branch solutions of the RY static structure factor, and the lower part to the low-charge solutions. For a given salt concentration C_s, the compressibility factor $S_f(q = 0)$ for most of the low-charge branch systems (corresponding to low λ values) is smaller than that of the high-charge branch systems (corresponding to high λ).

The horizontal solid line in the main figure represents the RY value $S_f(q = 0) = 0.0185$ calculated for a neutral hard-sphere system at freezing where $\phi = 0.494$. It coincides practically with the value of 0.0186 calculated directly from the Carnahan-Starling compressibility equation for hard spheres. Except for large values of the reduced screening parameter, the here considered masked-core Yukawa-particle systems at freezing are far less compressible. For the smallest

TABLE I. RY-HV predicted properties of masked-core Yukawa-particle systems at freezing.

λ	$\lambda < \lambda_t$[a]	λ_t[a] $< \lambda < 60$
$S(q_m)$	3.1 (imposed HV criterion)	3.1 (imposed HV criterion)
$S(q = 0)$	Small, down to 0.0006	Large, up to 0.018
$g_f(r_m)$	2.6, constant	2.6–4.3, increasing with λ
$\beta u_f(\langle r \rangle)$	$\gg 1$, $|u(r)|$ with small slope for long-range repulsion	<1 typically, decreasing with λ, large slope of $|u(r)|$, increasing with λ, short-range repulsion
$r_n/\langle r \rangle$	1.18—value expected for a small bcc crystal	1.13—value expected for a small fcc crystal
$(2\pi/q_m)/\langle r \rangle$	0.91—value expected for a small bcc crystal	0.88—value expected for a small fcc crystal
N_n	14—value expected for a small bcc crystal	12—value expected for fcc crystal
Crystal structure	bcc-like	fcc-like
Concentration	Only low-charge branch, all concentrations	All concentrations of high-charge branch and some concentrations of low-charge branch
Added salt concentration	$<20\ \mu$M (for this system)	All
Effective charge	Low-charge branch	Low- and high-charge branch

[a]Simulation predictions for the reduced screening parameter at the triple point vary between 6.9[35] and 7.7.[36]

considered value of $\lambda = 1.09$, the compressibility factor is $S_f(q = 0) = 0.0006$ which is about 30 times smaller than that of the hard-sphere system at freezing.

III. CONCLUSIONS

On basis of the RY liquid-state integral equation scheme and the fluid-phase Hansen-Verlet criterion with constant value $S_f(q_m) = 3.1$, we have given a thorough discussion on the behavior of the RDF and static structure factor of repulsive Yukawa-particles systems under freezing conditions. In addition we explored the behavior of the characteristic lengths associated with the Fourier transform pair. Our focus has been on Yukawa-system with masked hard-core and short-range attractions, which in $(\lambda, \tilde{T})$ space are characterized by a universal freezing line. As we have discussed in relation to Eqs. (3)–(6), this gives rise to universal lines for $g_f(r_m)$, $S_f(0)$, $r_m/\langle r \rangle$, $r_n/\langle r \rangle$, $2\pi/(q_m \langle r \rangle)$, and N_n as functions of λ.

While the local structure properties at freezing have been therefore analyzed mainly in their dependence on λ, in search for general scaling rules, we have additionally discussed these properties in terms of experimental control parameters for charge-stabilized silica spheres in DMF, including volume fraction and added salt concentration. This has allowed us to make contact with the experimental part in Paper I that triggered the present theoretical study.

Our study has revealed qualitative differences in the local structure of low-λ (Lλ, with $\lambda < \lambda_t$) and high-λ (Hλ, with $\lambda > \lambda_t$) systems at freezing, i.e., for systems located well inside the bcc and fcc segments, respectively, of the universal freezing line.

We showed in particular for Lλ systems that the pair interaction energy, $u_f(\langle r \rangle)$, at mean particle distance is large (5–40 k_BT) whereas the (negative) slope of $\beta u(r)$ is small, corresponding to a long-range soft repulsion. In contrast, $u_f(\langle r \rangle)$ is small for Hλ systems (i.e., 0.5–5 k_BT) but the slope of $\beta u(r)$ is now large, implying a shorter-range, less soft repulsion.

If plotted as function of r/r_m and q/q_m, the RY-HV RDF $g(r)$ and static structure factors $S(q)$ at freezing are, respectively, practically coincident for the Lλ systems, with practically constant RDF peak height $g(r_m) = 2.6$ close to the

value found at the isochoric bcc-fluid transition point of the one-component plasma. This translates into a likewise constant Ravache-Mountain-Streett ratio value $R_{RMS} = 0.23$, indicative of a freezing transition point for particles with very long-range repulsive interactions. In the high-λ regime, the RMS ratio decreases monotonically with increasing λ. One can thus not formulate a constant-value freezing criterion in terms of $g(r)$.

While for the Hλ systems the principal peak heights of $S(q)$ at freezing are identical, as enforced by the imposed HV rule, the principal peak position varies slightly with λ, as well as the other maxima and minima amplitudes and wavenumber locations. Significantly more pronounced are instead the differences in the RDF of the Hλ systems where the principal peak value $g_f(r_m)$ increases with increasing λ from 2.6 up to 4.3 at $\lambda = 60$.

Another parameter characterizing local order is the mean nearest neighbor distance r_n defined in Eq. (15) in terms of $g(r)$. This distance in units of $\langle r \rangle$ is a unique function of λ. In the Lλ and Hλ regions, the RY-HV prediction for r_n asymptotes nicely to plateau values obtained from MD simulations[31] of bcc and fcc crystals, respectively. These limiting plateau values of r_n are different from the nearest neighbor distances of an ideal bcc and fcc crystal, and in particular largely different from the Lλ and Hλ values taken by the RDF peak position r_m.

The RY-HV scheme result for the number of nearest neighbors, N_n, defined according to Eq. (16) with r_{dip} as upper integration cutoff, describes a smooth decline of this number from the Lλ plateau value 13.7 to a Hλ plateau region with $N_n = 11.7$. These limiting values are close to the values $N_n(\text{bcc2}) = 14$ and $N_n(\text{fcc}) = 12$ expected for a high-temperature bcc and fcc solid, respectively.

The major findings of this study are summarized in Table I, which serves as a quick reference for scientist dealing with charge-stabilized suspensions.

[1]S. John, Phys. Rev. Lett. **58**, 2486 (1987).

[2]P. N. Pusey and W. van Megen, Nature (London) **320**, 340 (1986).

[3]F. Westermeier, B. Fischer, W. Roseker, G. Grübel, G. Nägele, and M. Heinen, J. Chem. Phys. **137**, 114504 (2012).

[4]P. Holmqvist and G. Nägele, Phys. Rev. Lett. **104**, 058301 (2010).

[5]P. Holmqvist, P. S. Mohanty, G. Nägele, P. Schurtenberger, and M. Heinen, Phys. Rev. Lett. **109**, 048302 (2012).

[6]M. Heinen, F. Zanini, F. Roosen-Runge, D. Fedunová, F. Zhang, M. Hennig, T. Seydel, R. Schweins, M. Sztucki, M. Antalík, F. Schreiber, and G. Nägele, Soft Matter **8**, 1404 (2012).

[7]J. Gapinski, A. Wilk, A. Patkowski, W. Haeussler, A. J. Banchio, R. Pecora, and G. Nägele, J. Chem. Phys. **123**, 054708 (2005).

[8]A. Ivlev, H. Löwen, G. Morfill, and C. P. Royall, in *Complex Plasmas and Colloidal Dispersions: Particle-resolved Studies of Classical Liquids and Solids*, Series in Soft Condensed Matter Vol. 5, edited by D. Andelman and G. Reiter (World Scientific, Singapore, 2012).

[9]J. Gapinski, G. Nägele, and A. Patkowski, J. Chem. Phys. **136**, 024507 (2012).

[10]J. Gapinski, A. Patkowski, A. J. Banchio, J. Buitenhuis, P. Holmqvist, M. P. Lettinga, G. Meier, and G. Nägele, J. Chem. Phys. **130**, 084503 (2009).

[11]F. J. Rogers and D. A. Young, Phys. Rev. A **30**, 999 (1984).

[12]J.-P. Hansen and L. Verlet, Phys. Rev. **184**, 151 (1969).

[13]S. Zhou and X. Zhang, J. Phys. Chem. B **107**, 5294 (2003).

[14]F. A. Lindeman, Phys. Z. **11**, 609 (1910).

[15]H. J. Raveché, R. D. Mountian, and W. B. Streett, J. Chem. Phys. **61**, 1970 (1974).

[16]J.-P. Hansen and D. Schiff, Mol. Phys. **25**, 1281 (1973).

[17]H. R. Wendt and F. F. Abraham, Phys. Rev. Lett. **41**, 1244 (1978).

[18]P. V. Giaquinta and G. Giunta, Physica A **187**, 145 (1992).

[19]F. Saija, S. Prestipino, and P. Giaquinta, J. Chem. Phys. **124**, 244504 (2006).

[20]H. Löwen, T. Palberg, and R. Simon, Phys. Rev. Lett. **70**, 1557 (1993).

[21]O. S. Vaulina and S. A. Khrapak, J. Exp. Theor. Phys. **92**, 228 (2001).

[22]G. Nägele, M. Kollmann, R. Pesche, and A. J. Banchio, Mol. Phys. **100**, 2921 (2002).

[23]T. Palberg, W. Mönch, F. Bitzer, R. Piazza, and T. Bellini, Phys. Rev. Lett. **74**, 4555 (1995).

[24]L. F. Rojas-Ochoa, R. Castañeda-Priego, V. Lobaskin, A. Stradner, F. Scheffold, and P. Schurtenberger, Phys. Rev. Lett. **100**, 178304 (2008).

[25]O. Vaulina, S. Khrapak, and G. Morfill, Phys. Rev. E **66**, 016404 (2002).

[26]D. Gottwald, C. N. Likos, G. Kahl, and H. Löwen, J. Chem. Phys. **122**, 074903 (2005).

[27]J. Riest, P. Mohanty, P. Schurtenberger, and C. N. Likos, Z. Phys. Chem. **226**, 711 (2012).

[28]P. Wette, I. Klassen, D. Holland-Moritz, T. Palberg, S. V. Roth, and D. M. Herlach, Phys. Rev. E **79**, 010501 (2009).

[29]P. Wette, I. Klassen, D. Holland-Moritz, D. M. Herlach, H. J. Schöpe, N. Lorenz, H. Reiber, T. Palberg, and S. V. Roth, J. Chem. Phys. **132**, 131102 (2010).

[30]D. M. Herlach, I. Klassen, P. Wette, and D. Holland-Moritz, J. Phys.: Condens. Matter **22**, 153101 (2010).

[31]O. Robbins, K. Kremer, and G. S. Grest, J. Chem. Phys. **88**, 3286 (1988).

[32]K. Kremer, M. O. Robbins, and G. S. Grest, Phys. Rev. Lett. **57**, 2694 (1986).

[33]E. J. Meijer and D. Frenkel, J. Chem. Phys. **94**, 2269 (1991).

[34]M. J. Stevens and M. O. Robbins, J. Chem Phys. **98**, 2319 (1993).

[35]S. Hamaguchi, R. T. Farouki, and D. H. E. Dubin, Phys. Rev. E **56**, 4671 (1997).

[36]R. S. Hoy and M. O. Robbins, Phys. Rev. E **69**, 056103 (2004).

[37]D. C. Wang and A. P. Gast, J. Chem. Phys. **112**, 2826 (2000).

[38]A. J. Archer, Phys. Rev. E **72**, 051501 (2005).

[39]M. Heinen, P. Holmqvist, A. J. Banchio, and G. Nägele, J. Chem. Phys. **134**, 044532 (2011).

[40]J. Liu, H. J. Schöpe, and T. Palberg, J. Chem. Phys. **116**, 5901 (2002).

[41]S. H. Behrens and M. Borkovec, J. Chem. Phys. **111**, 382 (1999).

[42]F. Carrique, F. J. Arroyo, M. L. Jiménez, and A. V. Delgado, J. Chem. Phys. **118**, 1945 (2003).

[43]K. van Gruijthuijsen, M. Obiols-Rabasa, M. Heinen, G. Nägele, and A. Stradner, Langmuir **29**, 11199 (2013).

[44]M. Evstigneev, O. Zvyagolskaya, S. Bleil, R. Eichhorn, C. Bechinger, and P. Reimann, Phys. Rev. E **77**, 041107 (2008).

[45]D. Hessinger, M. Evers, and T. Palberg, Phys. Rev. E **61**, 5493 (2000).

[46]P. Wette, H. J. Schöpe, and T. Palberg, Colloids Surf. A **222**, 311 (2003).

[47]L. Shapran, M. Medebach, P. Wette, T. Palberg, H. J. Schöpe, J. Horbach, T. Kreer, and A. Chatterji, Colloids Surf. A **270–271**, 220 (2005).

[48]S. Alexander, P. M. Chaikin, P. Grant, G. J. Morales, and P. Pincus, J. Chem. Phys. **80**, 5776 (1984).

[49]L. Belloni, Colloids Surf. A **140**, 227 (1998).

[50]A. Torres, G. Téllez, and R. van Roij, J. Chem. Phys. **128**, 154906 (2008).

[51]T. E. Colla, Y. Levin, and E. Trizac, J. Chem. Phys. **131**, 074115 (2009).

[52]J. M. Falcón-González and R. Castañeda-Priego, Phys. Rev. E **83**, 041401 (2011).

[53]A. P. dos Santos, A. Diehl, and Y. Levin, Langmuir **26**, 10778 (2010).

[54]R. Roa, F. Carrique, and E. Ruiz-Reina, Phys. Chem. Chem. Phys. **13**, 19437 (2011).

[55]M. Heinen, T. Palberg, and H. Löwen, J. Chem. Phys. **140**, 124904 (2014).

[56]J. K. Phalakornkul, A. P. Gast, R. Pecora, G. Nägele, A. Ferrante, B. Mandl-Steininger, and R. Klein, Phys. Rev. E **54**, 661 (1996).

[57]A. J. Schmid, J. Riest, T. Eckert, P. Lindner, G. Nägele, and W. Richtering, "Comparison of the microstructure of stimuli responsive zwitterionic PNIPAM-co-sulfobetaine microgels with PNIPAM microgels and classical hard-sphere systems," Z. Phys. Chem. (in press).

[58]T. Palberg, T. Köller, B. Sieber, H. Schweinfurth, H. Reiber, and G. Nägele, J. Phys.: Condens. Matter **24**, 464109 (2012).

[59]Y. Monovoukas and A. P. Gast, J. Coll. Int. Sci. **128**, 533 (1989).

[60]T. Palberg, J. Phys.: Condens. Matter **11**, R323–R360 (1999).

[61]H. Graf and H. Löwen, Phys. Rev. E **57**, 5744 (1998).

[62]D. C. Wang and A. P. Gast, J. Phys.: Condens. Matter **11**, 10133 (1999).

[63]M. Heinen, E. Allahyarov, and H. Löwen, J. Comput. Chem. **35**, 275 (2014).

[64]A. J. Greenfield, J. Wellendorf, and N. Wiser, Phys. Rev. A **4**, 1607 (1971).

[65]J. M. Stallard and C. M. Davis, Phys. Rev. A **8**, 368 (1973).